A study of the onset of melt over the Arctic Ocean in RADARSAT synthetic aperture radar data

R. Kwok, G. F. Cunningham, and S. V. Nghiem

Jet Propulsion Laboratory, California Institute of Technology, Pasadena, California, USA

Received 26 February 2002; revised 20 September 2002; accepted 23 December 2002; published 26 November 2003.

[1] The regional melt onset signal of Lagrangian elements of Arctic sea ice in RADARSAT synthetic aperture radar (SAR) data during the spring of 1998 is examined. The melt signal is clearly detectable not only in backscatter changes over multiyear ice but also first-year ice and mixtures of these ice types. This allows a more complete mapping of the progression of melt over the sea ice cover. For the spring of 1998 the onset dates range between 10 May and 29 June. The spatial pattern of melt onset is characterized by sharp boundaries delineating distinct regions with relatively uniform onset dates. This pattern appears to be associated with moisture and warm air brought in by a low-pressure trough and the timing of a rain event reported at the Surface Heat Budget of the Arctic Ocean (SHEBA) camp. Measurements from the SHEBA camp show good correspondence between the timing of melt in SAR imagery and the onset of albedo drop off associated with the beginning of summer. Onset dates are compared with the timing of the zero crossing of the temperature records from drifting buoys and the onset dates derived from satellite passive microwave brightness temperature fields. The timing of our estimates is within 1–2 days of the zero crossing of the buoy temperature records. Onset dates derived from passive microwave observations appear to be biased toward a later stage of melt. Comparison with results derived from a SAR data set from the spring of 1992 show that the onset of melt in 1998, derived from RADARSAT, in the Beaufort Sea occurred 2 weeks earlier. *INDEX TERMS:* 4540 Oceanography: Physical: Ice mechanics and air/sea/ice exchange processes; 4207 Oceanography: General: Arctic and Antarctic oceanography; 4227 Oceanography: General: Diurnal, seasonal, and annual cycles; 4275 Oceanography: General: Remote sensing and electromagnetic processes (0689); *KEYWORDS:* melt onset, Arctic ice cover, radar remote sensing, Lagrangian ice motion

Citation: Kwok, R., G. F. Cunningham, and S. V. Nghiem, A study of the onset of melt over the Arctic Ocean in RADARSAT synthetic aperture radar data, *J. Geophys. Res.*, *108*(C11), 3363, doi:10.1029/2002JC001363, 2003.

1. Introduction

[2] The dramatic decrease in the total albedo of the sea ice cover that accompanies the onset of snowmelt is clearly illustrated in Figure 1. Over the Arctic Ocean sea ice cover, this is associated with the appearance of liquid water in the snow cover as the air temperature approaches 0°C. This large decrease in surface albedo increases the absorption and heating of the ice by shortwave radiation and significantly affects the surface energy balance. On a broader context, this marks the end of the ice growth season and the beginning of summer. Changes in the timing and spatial patterns of the onset of the melt season are important parameters in polar climate studies and these trends may serve as sensitive indicators of longer-term climate change in the high latitudes.

[3] The detection of the timing of melt onset in satellite microwave observations utilizes the significant changes in the microwave emissions or backscatter during this seasonal transition. There is, in general, a sharp increase in the passive microwave emissivity that can be observed in the scanning multichannel microwave radiometer (SMMR) and special sensor microwave imager (SSM/I) brightness temperature fields. The long record of satellite passive microwave data has been used, with some success, to detect and study the large-scale pattern of melt onset [*Anderson*, 1987, 1997; *Smith*, 1998; *Anderson and Drobot*, 2001; *Drobot and Anderson*, 2001a, 2001b]. Interpretation of the variability of the melt signal is, however, more difficult because of the coarse spatial resolution of the sensors. Specifically, the time series of brightness temperatures at fixed geographic locations in the gridded fields consist of contributions from varying areal fractions of different ice types and open water because of divergence and advection of sea ice. Other sources of variability that affect the brightness temperature measurements include variations in atmospheric water vapor and liquid water and variations in surface temperature.

[4] The higher spatial resolution of synthetic aperture radar (SAR) observations, on the order of 100 m, permits a more detailed examination of the temporal signature

0148-0227/03/2002JC001363$09.00

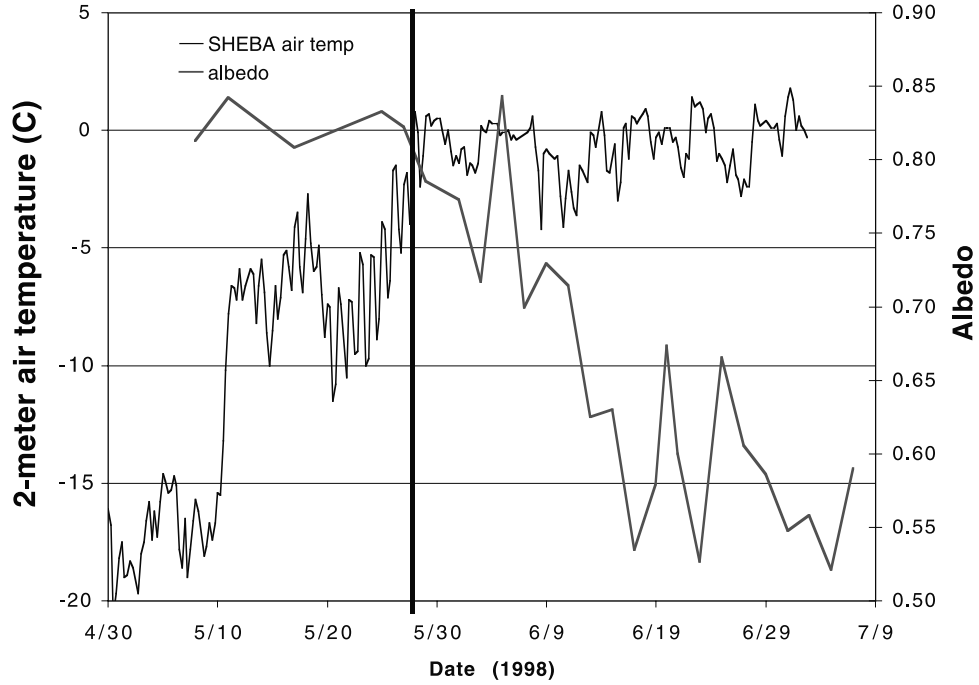

Figure 1. The dependence of total albedo on surface air temperature measured near the SHEBA camp during melt onset in 1998 [*Perovich et al.*, 1999]. The vertical line indicates the timing of melt onset estimated from RADARSAT SAR data.

changes of individual ice types. An additional merit of the lower-frequency SAR data is that they are relatively insensitive to atmospheric perturbations. *Winebrenner et al.* [1994] showed that the onset of melt and freeze-up events are clearly detectable as changes in the backscatter of multiyear ice (MY) in ERS-1 imagery. During melt onset, liquid water in the snow cover on MY ice is marked by a steep decrease (almost 9dB) in the observed backscatter. In contrast, *Barber et al.* [1995] finds an increase in first-year backscatter associated with the onset of melt. A simple procedure using backscatter/albedo relation to construct thematic maps of backscatter derived surface albedo was proposed by *Thomas and Barber* [1998]. However, until the launch of RADARSAT in November of 1995, the potential use of high-resolution radar data for monitoring the Arctic sea ice cover has not been realized because of the relatively poor temporal coverage offered by the European ERS satellites.

[5] The 24-day orbit cycle of the RADARSAT satellite and the wide-swath imaging mode (460 km) of the C band radar provide near repeat coverage of the entire Arctic Ocean every 3–6 days. In anticipation of these capabilities of RADARSAT, *Kwok et al.* [1995] suggested a scheme to use the available temporal and spatial coverage of the radar to obtain estimates of ice deformation and ice thickness using systematic Lagrangian observations of ice motion. The motivation is to derive basin-scale estimates of geophysical fields that are suitable for process studies, model validation, and climatological studies. The scheme follows Lagrangian elements of sea ice and permits us to monitor the changes in the area and backscatter of specific ice parcels over time. The backscatter history of these elements is unique in that they contain the same ice differing only by an amount due to deformation or growth/melt. Beginning in November of 1996 and continuing today, 3-day RADARSAT maps of the western Arctic Ocean within the Alaska SAR Facility (ASF) reception mask are being acquired. The SAR imagery are used as inputs into a system know as the RADARSAT Geophysical Processor System (RGPS) [*Kwok*, 1998] that produces temporal records of deformation and backscatter for material elements initially 10 km on a side. The RGPS data set includes sequences of observations that span the entire period of melt onset. Within each Lagrangian element, the data set provides estimates of the divergence, the fractional coverage of first-year and multiyear ice, and the backscatter distribution of the sample population. As the RGPS elements move with the ice cover, the ice within the area remains the same differing only by an amount due to deformation (opening and closing) or melt.

[6] In this paper, we examine the melt onset signal in the record of SAR backscatter observations produced by the RGPS. The discussions here focus on a detailed examination of spatial and temporal dependence of the melt signal in C band SAR data, the approach used to determine the timing of melt onset, and the comparison of timing of melt onset with results from in situ and other satellite observations. In the next section, we provide a brief description of the RGPS data set and its coverage during the melt onset period in 1998. In Section 3, we show the backscatter record of three Lagrangian elements from different locations in the Arctic Ocean. The observed dependence of the onset signal on ice type mixtures over the Arctic Ocean is discussed. In Section 4, we examine the results of our melt onset analysis. The spatial pattern of melt onset for 1998 and comparisons of these results with buoy temperature records and onset timing from SSM/I data are discussed. The final section

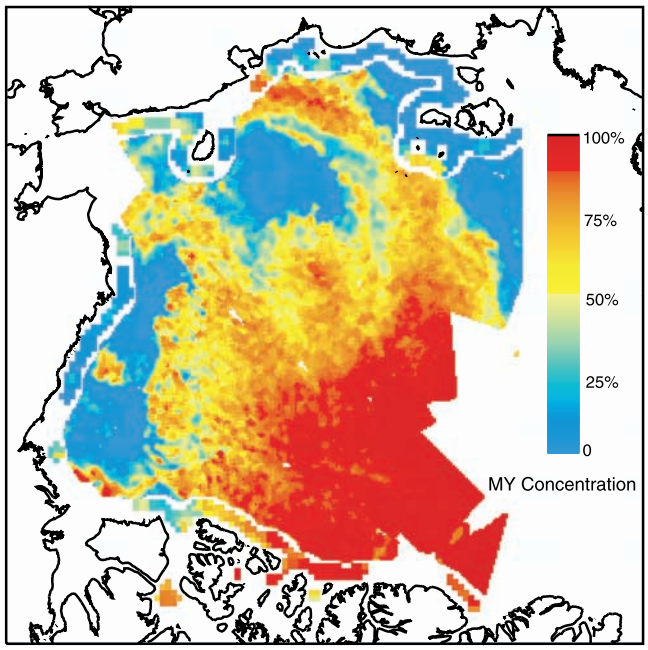

Figure 2. The coverage of the Arctic Ocean by RGPS Lagrangian elements and the multiyear ice fraction within each element between days 130 and 140. There are approximately 23,488 cells covering the domain.

summarizes the paper. Appendix A outlines the procedure to detect the timing of melt onset on the basis of the phenomenology discussed in this paper.

2. Data Description

[7] In our study, we employ the RGPS observations from the period between May and July of 1998. The scheme for tracking the Lagrangian elements (cells) in RADARSAT imagery was initialized on 10 May 1998 using 23,488 cells of ~10 km on a side covering an area of $\sim 2.43 \times 10^6$ km^2. Line segments connecting the four vertices of a cell define its boundaries. At startup, each cell has a sample population of 100 by 100 image samples with pixel spacing of 100 m. Coastal sea ice (within 100 km of land) is sampled by 533 larger cells (25 km by 25 km), covering $\sim 0.34 \times 10^6$ km^2, as tracking ice features in these areas is more difficult. This selection is based solely on computational considerations. The spatial coverage of the RGPS cells is shown in Figure 2. The repeat sampling of each cell is nominally 3 days, but can vary between 1 and 15 days depending on data acquisition opportunities.

[8] From the RGPS data set, we obtain a sequence of observations containing geographic locations, multiyear (MY) ice coverage, cell areas, 2-m air temperatures, and the backscatter distributions of the sample population within each cell. An ice motion tracker in the RGPS system provides the location of the cell vertices by identifying common features in the time sequential imagery. Comparison of RGPS and buoy displacements gives an RMS difference of ~100–300 m. Locally, where the geolocation uncertainties between two images are correlated, the calculation of spatial differences to determine deformation is not dependent on the geolocation error of the data. *Kwok and Cunningham* [2002] estimate an uncertainty in the area calculations to be ~1–2%. The MY ice (sea ice that has survived at least one summer's melt) coverage within each cell is estimated using a maximum likelihood classifier and tabulated values of the expected backscattering cross section of MY ice and first-year (FY) ice [*Kwok et al.*, 1995]. The table contains a coarse description of the spatial dependence and the approximate incidence angle dependence of the backscatter of the two ice types determined from RADARSAT observations. An image pixel is assigned to one of two ice types: multiyear or first year. The classification scheme also allows for uncertainty in radar calibration by allowing for moderate drifts (±2 dB) in the estimated backscatter in the RADARSAT image data processed at ASF.

[9] The incidence angles across the wide swath of the RADARSAT imagery range from 20°–50°. The backscatter estimates used here are all referenced to an angle of 30° using the incidence angle dependence data mentioned above. Only descending imaging passes, where the RADARSAT satellite crosses the equator at approximately 6:00AM local time, are used here. This ensures that the observations within a time series are all collected at approximately the same local time and thus at the same point in the diurnal cycle. Diurnal changes in the backscatter can be significant over the range of incidence angle of RADARSAT SAR data [*Nghiem and Bertoia*, 2001].

[10] Temperature records from individual International Arctic Buoy Program (IABP) buoys are used here. Also, the gridded (100 km) 2-m air temperature fields from the optimally interpolated IABP/Polar Exchange at the Sea Surface (IABP/POLES) surface air temperature data set [*Rigor et al.*, 2000] are used in the detection algorithm. Air temperatures at the center of RGPS cells are obtained by interpolation of these fields. The correlation length scales of the temperature fields are quite large, ranging from 1000 km in the fall, winter, and spring to 300 km in the summer. Thus negligible error is incurred in the interpolation process.

3. Onset of Melt in C Band SAR Data

[11] To illustrate the backscatter behavior during onset, we first show sequences of SAR imagery at three separate locations over the Arctic Ocean for a 10–15 day period around the onset date (Figure 3). The imagery includes an area from the high Arctic (~83°N), an area around the Surface Heat Budget of the Arctic Ocean (SHEBA) ice camp (~76.7°N), and an area with mostly FY ice (~74°N). The dependence of the signal of melt onset on the fraction of MY and FY ice using the summary statistics gathered from the entire RGPS cell population is then discussed.

3.1. Measures of Melt Onset

[12] Three metrics (σ, f, and P) derived from the backscatter distribution of each cell are used (see Appendix A for specific details on each metric). The backscatter signal (σ) representing the average over the area (5 km × 5 km) and the temperature record from the closest IABP buoy is shown on the first row of Figure 4. The second panel shows a parameter, f, defined as the fractional cell area (0–100%) with backscatter above a threshold, σ_{th}. To compute this threshold, two backscatter centroids are first derived from

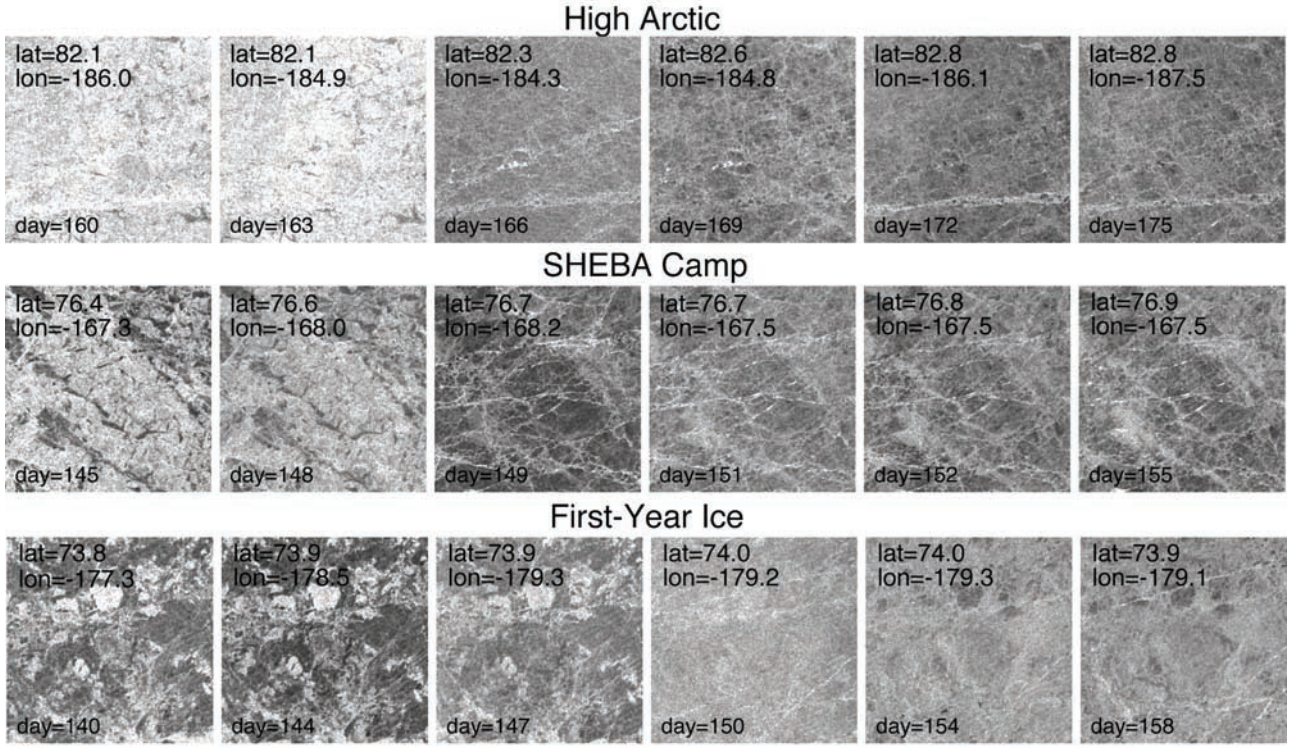

Figure 3. Sequences of SAR imagery showing the backscatter behavior (C band) over three sample areas approximately 50 km on a side: (a) a region located in the high Arctic of mostly multiyear ice, (b) a region centered around the SHEBA ice camp, and (c) an area with a higher fraction of first-year ice. The geographic location of the image center and the day of acquisition of the imagery are shown within each box. (RADARSAT imagery ©CSA 2001) Gray levels in the images are proportional to backscatter intensity.

each RGPS cell population using a cluster analysis procedure (ISODATA) [*Ball and Hall*, 1967]. The centroid closest to the tabulated MY backscatter used in the ice classification procedure described earlier is then assumed to be the mean MY ice backscatter for that cell. σ_{th} is defined as -3.5 dB from this value. This dynamic threshold for each cell allows for some variability in the calibration of the radar data and the spatial variability of MY backscatter at different locations in the Arctic. As the backscatter distribution of the cell population increases or decreases during onset, this gives a consistent measure of the area within a cell affected by melt. The third panel shows the relative density at the peak, P, of the backscatter histogram of a cell. During melt onset, P measures the relative "peakiness" of the histogram. Discussed later, we find this metric to be effective in detecting melt onset when mixtures of ice types are present in the sample population.

3.2. Three Sample Areas

3.2.1. High Arctic

[13] In the image sequences (Figure 3), multiyear ice with its relatively high backscatter (typically >4 dB above that of FY ice) is easily identified in SAR imagery prior to melt onset. At this high latitude (>82°N), the coverage by MY ice is >97%. A map of the MY ice coverage of the region covered by RGPS cells before melt onset is shown in Figure 2. When temperatures are below freezing between mid-May and early June (Figure 4), the mean backscatter of the sample population remains stable at ~ -10 dB. A decrease in the backscatter of $\sim$4 dB can be seen on day 165 (14 June) as the temperature rose and stayed above freezing. After this date, the area-averaged backscatter stays below -13 dB. This is the onset signal that is characteristic over areas with predominantly MY ice. The physical basis for this steep decrease is due solely to the appearance of liquid water in the snow cover causing attenuation of the radar backscatter [*Winebrenner et al.*, 1994]. The behavior of the three metrics over this period can be seen in Figure 4. In addition to the decrease in mean backscatter, a significant and definitive shift in the sample population toward lower backscatter, as measured by f, is evident. Changes in P during onset are, however, not remarkable since all the MY samples within the RGPS cell experiences a uniform decrease in backscatter.

3.2.2. SHEBA Camp

[14] This area is of particular interest as it coincides with the location of the year-long SHEBA camp [*Perovich et al.*, 1999] and the availability of albedo measurements during this period. The evolution of wavelength-integrated albedos sampled along a 100 m line near the camp can be seen in Figure 1. We briefly summarize the description of the albedo record given by *Perovich et al.* [1999]. Measurements from the cold snow covered ice of 17 April (day 107) show that the albedo is high (0.85) and spatially uniform. This high and spatially uniform albedo persisted for the next several weeks. A month later, on 25 May, no melting had

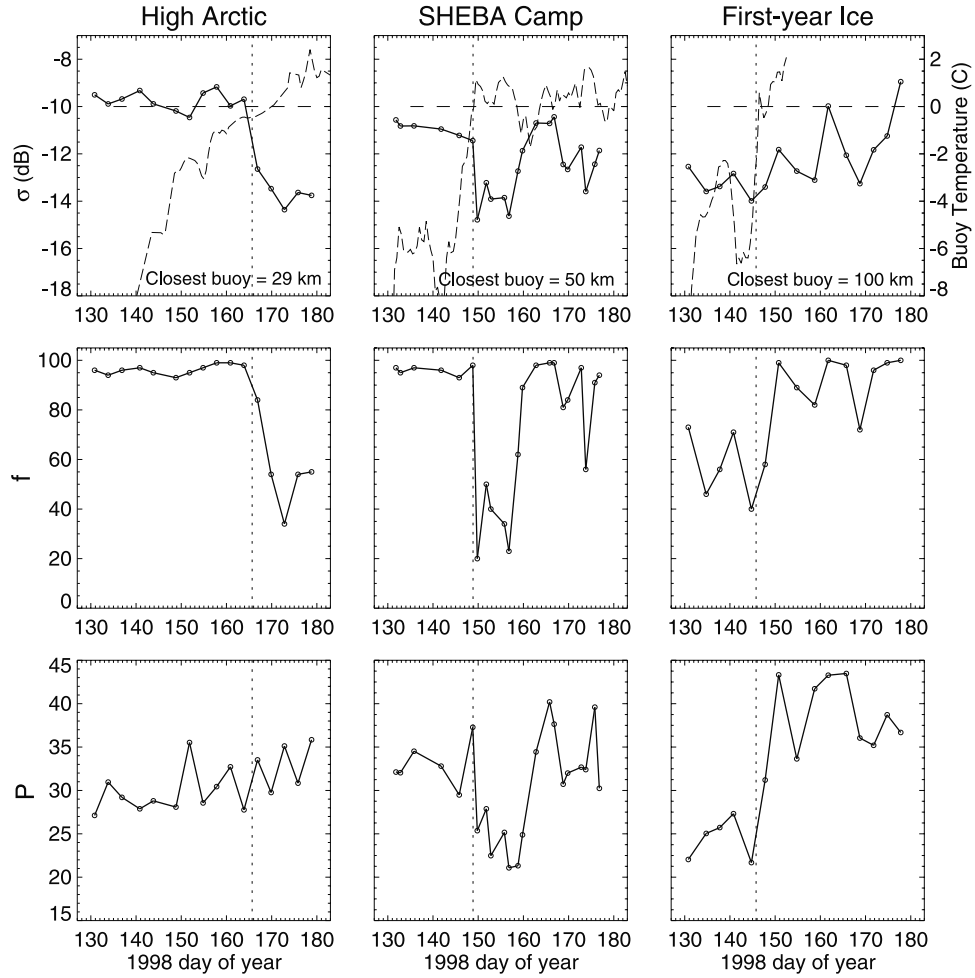

Figure 4. The behavior of the three indicators (σ, *f*, and *P*) of melt onset within 5 km windows centered over the three sample areas shown in Figure 2: (a) σ, normalized backscatter; (b) *f*, fractional change in area above a dynamic threshold; and (c) *P*, peak of the backscatter histogram. The dashed line shows the temperature record from the closest IABP buoy. The distance to the closest buoy is indicated. Dashed vertical lines show the onset date estimated from RGPS data.

occurred, and the snow was still dry. Snow metamorphism during this time resulted in slightly larger grain sizes and a slight decrease in albedo. Rain on 29 May (day 149) marked the beginning of the melt season and a transition from dry snow to wet, melting snow. Measurements from 3 June show the albedo dropped to wet snow values of 0.7 to 0.75. In some places, the snow was no longer optically thick, resulting in a modest amount of spatial variability in albedo (∼0.1). Melting of the snowpack continued, and by 15 June the albedo line consisted of melting snow, bare melting ice, and a few melt ponds. Spatial variability along the line increased greatly, with albedo ranging from 0.3 for the ponds to 0.7 for the melting snow. The decrease in radar backscatter associated with the albedo drop on 29 May (during melt onset) is modest at ∼4 dB. This is accompanied by a decrease in *P* and a larger decrease in *f*. In this case, the changes in the three metrics seem to be good indicators of onset. The MY ice fraction of the sample population, at 95%, is lower compared to the previous example. The onset date (day 149) detected in the SAR image sequence corresponds to the date rain was reported over the SHEBA camp.

3.2.3. First-Year Ice

[15] The MY ice fraction over this 5 km window is ∼50%. Outside the window, the MY ice backscatter serves as a contrast to the behavior of FY ice backscatter. Prior to onset, the mean backscatter of the FY/MY mixture is ∼−13 dB. By itself, FY ice backscatter hovers around −16 dB. The sharp rise in buoy temperature around 26 May (day 146) should mark the onset of melt; however, no significant change in the backscatter signal is observed. This can be attributed to the different backscatter behavior of FY and MY ice during onset. For FY ice, an increase in backscatter is associated with melt onset compared to the characteristic steep decrease seen in MY ice. The reversal and reduction in contrast with FY ice having a higher backscatter can be seen clearly in Figure 3. As the backscatter of the ice types converges, significant changes in the mean backscatter of the population are not evident. However, a >50% increase in *f* results from the increase in backscatter of FY ice. The increase in *P* (∼20%) is an indication of the decrease in the variability of the backscatter and increase in the histogram peak (see Figure 5) as the characteristic surface backscatter of the cell population is

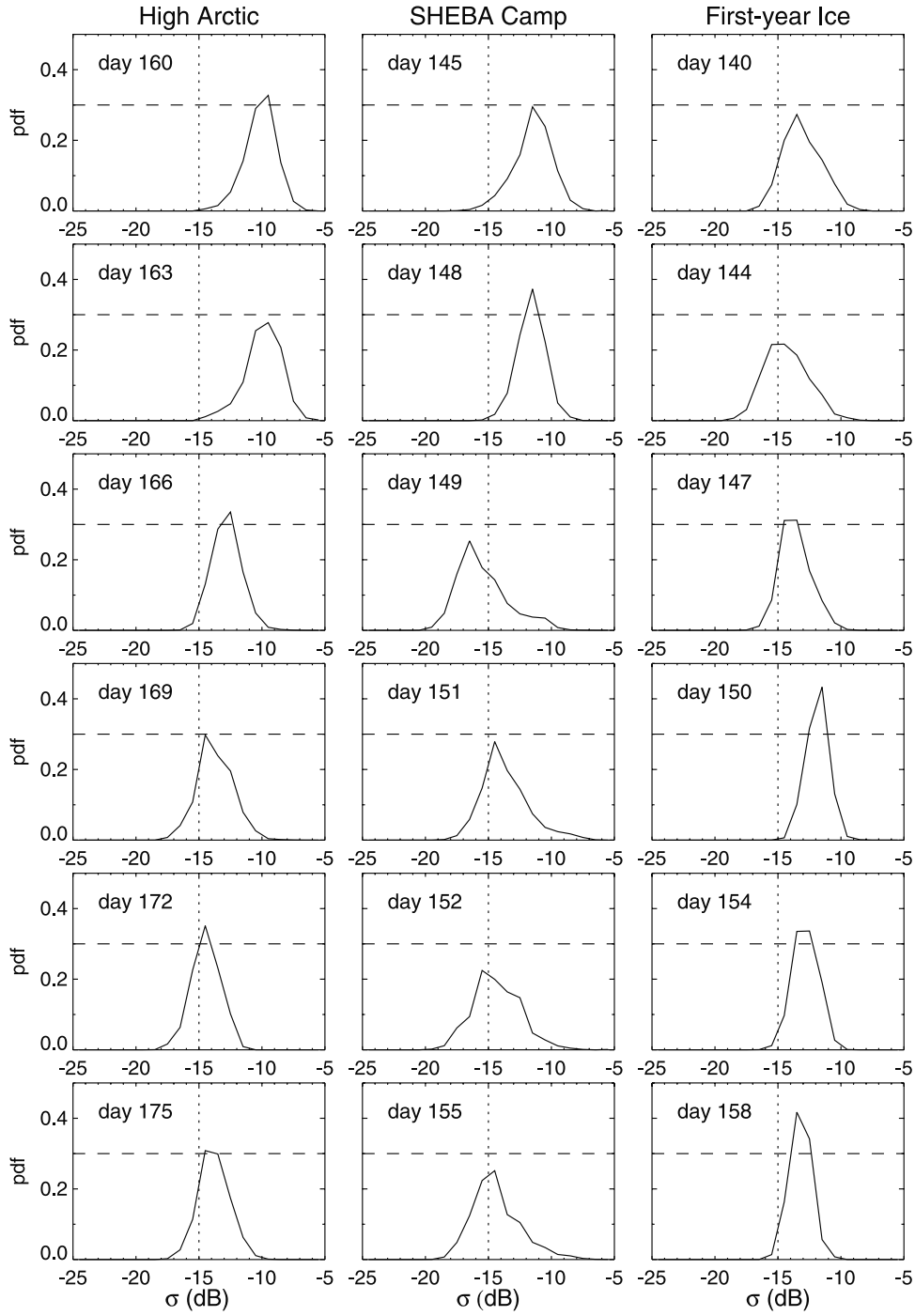

Figure 5. The changes in backscatter histograms (quantization level: 1 dB) of the three sample areas around the date of melt onset. The steep drop in backscatter is clearly indicated in the histograms of the high Arctic region and near the SHEBA camp. Over the area with ~50% FY ice, the onset is indicated instead by the sharpening of the backscatter histogram.

now masked by melt and the resultant backscatter converges to that from a surface with wet snow. This is a distinctive onset signal of RGPS cells with mixtures of FY and MY ice.

3.3. Variability of Melt Signal and Multiyear Ice Fraction

[16] Here, we examine in more detail the dependence of the melt signal on MY ice fraction (C_{MY}) using the entire RGPS cell population of 23,488 cells. We plot the average melt signal, as measured by the three indicators described above, within ten ranges of C_{MY} from 0–100% (Figure 6). The melt signature, in each range, represents the average of all the melt signals centered on the melt date as detected by the algorithm briefly described in the next section and detailed in Appendix A. Cells with divergence or convergence >25% during the period are excluded in the averaging

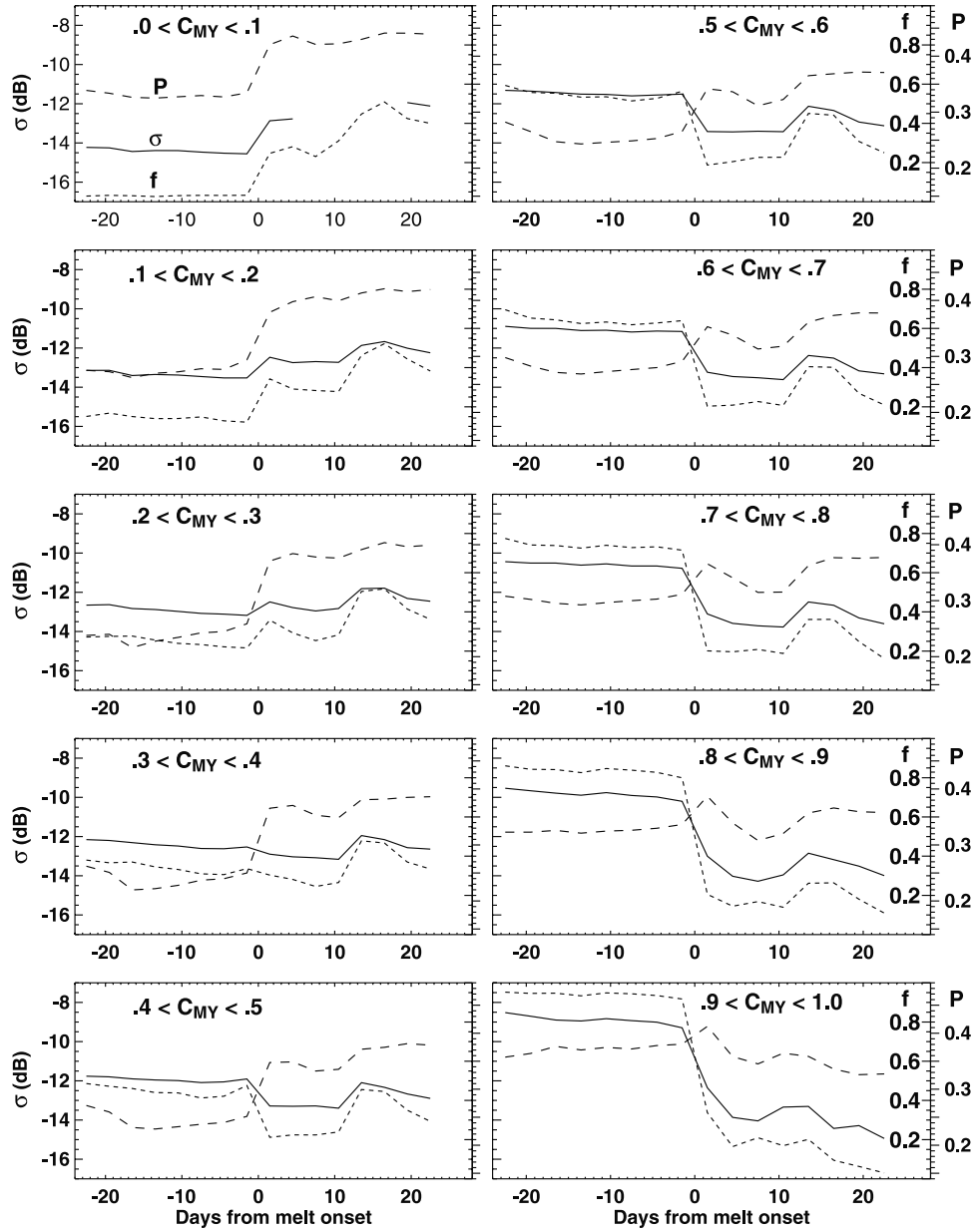

Figure 6. Dependence of melt onset signal on the multiyear ice fraction (C_{MY}). The mean temporal behavior of the three indicators (σ, *f*, and *P*) within each C_{MY} bin is created by averaging their records centered on the onset date.

process. This is to avoid contamination of the onset signatures from open water areas and to a lesser extent from the backscatter of new ridges. Also, cells with observational gaps >7 days are excluded as the sampling interval introduces too large of an uncertainty in the onset date.

[17] The melt signature of areas with more than 90% MY ice or FY ice are distinct and serve as a guide for understanding the melt signal of RGPS cells with mixtures of ice types. The backscatter of all cells remains stable up to the point of melt onset, with the mean cell backscatter intensity indicative of the approximate areal fractions of FY and MY ice. Prior to melt onset, the mean backscatter of 'pure' MY and FY ice areas are ∼−9 dB and ∼−14 dB, a contrast of ∼5 dB. RGPS cells with mixtures of MY and FY ice have mean backscatter between those values. The melt signal with its steep drop in the backscatter is clear when a cell has high C_{MY}. In cells with little MY ice, the signal is a rather less dramatic increase (∼2 dB), instead of decrease, in the mean backscatter. A clearer expression of the melt signal in these cases can be seen in the steep increases in *f* and *P*. Three weeks after melt, the mean backscatter of 'pure' MY and FY ice areas are −15 dB and −12 dB, a reversal and a reduction of contrast of ∼3 dB. This represents a large reduction in the contrast between the two ice types as the dominant scattering mechanisms responsible for their winter contrast are masked by surface melt processes. These changes can be easily seen in the imagery in Figure 3.

[18] With a mixture of MY and FY ice in the cell population, the melt signal is intermediate to that of areas with pure ice types. Figure 7 summarizes the changes and thus the

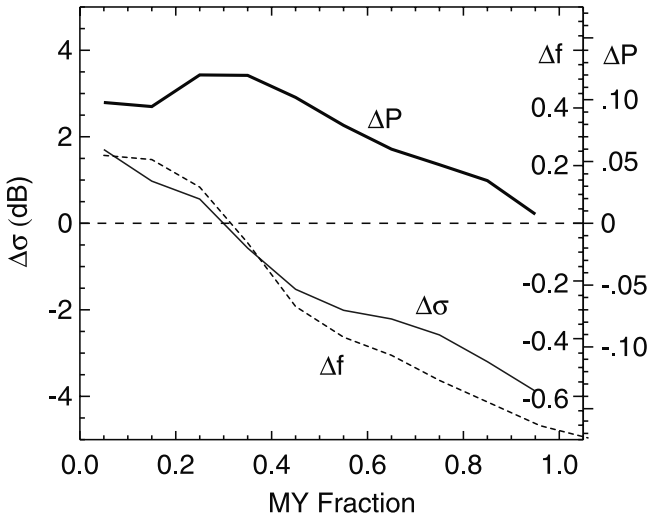

Figure 7. Dependence of the change in three indicators ($\Delta\sigma$, Δf, and ΔP) at melt onset on the multiyear fraction within each cell.

effectiveness of the three measures as indicators of melt onset. The dependence of the changes, in the magnitude of the three metrics during melt onset, on C_{MY} is evident. Here σ and f have very little sensitivity to melt when C_{MY} is between 20 and 40%. As discussed above, this is a consequence of the reversal and reduction in contrast between MY and FY ice after melt onset. Changes in σ and f are more significant at higher MY ice concentration. The increase in P during melt onset, however, stays fairly robust in regions with low MY concentration up to 50%. Again, the increase in P is an indication of the decrease in the backscatter variance of the cell population. The sensitivity of the three metrics and their dependence on C_{MY} is clearly indicated in Figure 6. This onset behavior is used in the design of the detection scheme.

[19] We note a postmelt phenomenon on the plots in Figure 6. Several days after onset, the temperature becomes nearly constant and hovers around freezing indicating the beginning of the melt season. A postmelt signal marked by a bump of ~1 dB appearing approximately 10 days after the onset of melt is a characteristic that is ubiquitous in all the plots. *Barber et al.* [1995] suggest that this increase results from the complete ablation of the snow cover from a slushy basal layer to a wet ice surface with melt ponds and the subsequent decrease is associated with drainage of the melt ponds. Regardless of the cause, it is interesting to note that this is a widespread phenomenon affecting different surface types over the ice cover of the Arctic Ocean.

4. Timing of Melt Onset

4.1. Melt Onset Detection Algorithm

[20] The design of the automatic melt onset detection algorithm is based on the sensitivity of the changes in the three metrics (σ, f, and P) at melt onset and their dependence on C_{MY}. Figure 7 serves as a model of the behavior of melt onset and a guide for designing the decision rules for detection procedures. The implementation details can be found in Appendix A. Suffice to say that the detection thresholds for $\Delta\sigma$, Δf, and ΔP are dependent on C_{MY} and are selected to minimize the detection noise or false alarms. The detected changes in the backscatter record represent the first significant event in the time series. The detection procedure does not appear to be sensitive to episodic cycling of the backscatter due to cooling and other processes associated after this event. In this section, we focus on the results of the detection process by comparison of the spatial timing of onset with other data sets and examination of the spatial pattern over the Arctic Ocean.

4.2. Spatial Pattern of Melt Onset Dates

[21] Figure 8 shows a map of the timing of melt onset and the distribution of these dates for the spring of 1998 estimated by the automatic algorithm. These indicators seem robust; the map of the timing is relatively smooth with no distinguishable boundaries between regions with predominantly FY and MY ice. Within the area with RGPS coverage, the onset dates ranges from day 130–180, or 10 May to 29 June. The spatial pattern of melt dates shows approximately three distinct regions with relatively uniform onset dates (145–150, 150–155, and 162–166). The spatial pattern is highly coherent and there is a fairly sharp boundary delineating the three regions. In late May, melt onset occurred over a large part of the Canada Basin east of Wrangel Island except that part of our study area west of Ellesmere island and north of Greenland. The other two regions experienced onset at later dates. At the SHEBA ice camp, the estimated date of melt onset is 29 May (day 149) and corresponds to the initial drop in albedo and the approximate zero crossing of the near surface air temperature measured at the ice camp (Figure 1). On the large scale, the second region to experience melt onset is the area west of Ellesmere, and the last region is the area west of Wrangel Island.

[22] The sharp boundaries between regions with relatively uniform onset dates in 1998 seen in the RGPS (Figure 8) and passive microwave estimates (described in the next section and seen in Figure 9) are interesting. The climatological south-north progression of onset is not as clear during this year. A possible cause of this unexpected melt onset pattern can be seen in the daily time series of 85 GHz (horizontal polarization) SSM/I brightness temperature fields with overlaid NCEP sea level pressure contours covering the time period 26 May through 6 June (Figure 10). The sequence begins (day 146) with an extensive high-pressure system covering the Beaufort Sea with what appears in the SSM/I image to be relatively dry region (low brightness temperatures) throughout the region. The subsequent 5 days show a low-pressure system moving northward into the region from Siberia. Of interest is an associated trough on the eastern side of the low traveling northward through the region, especially evident on day 149 and day 150. Note particularly that an area of high SSM/I brightness temperature is highly correlated with the location of the moving trough of low pressure. The region of high brightness temperature also corresponds with the timing of rain event at the SHEBA Camp site and with the timing of melt onset within this region seen in Figure 8. Also, the western edge of this brightness temperature feature (day 149 and day 150) corresponds very closely to the boundary of melt onset dates previously noted. The image for day 151 shows the eastern limit of the influence of this area of moisture. A different atmospheric system is then seen in day 152 through day 157 moving northward across

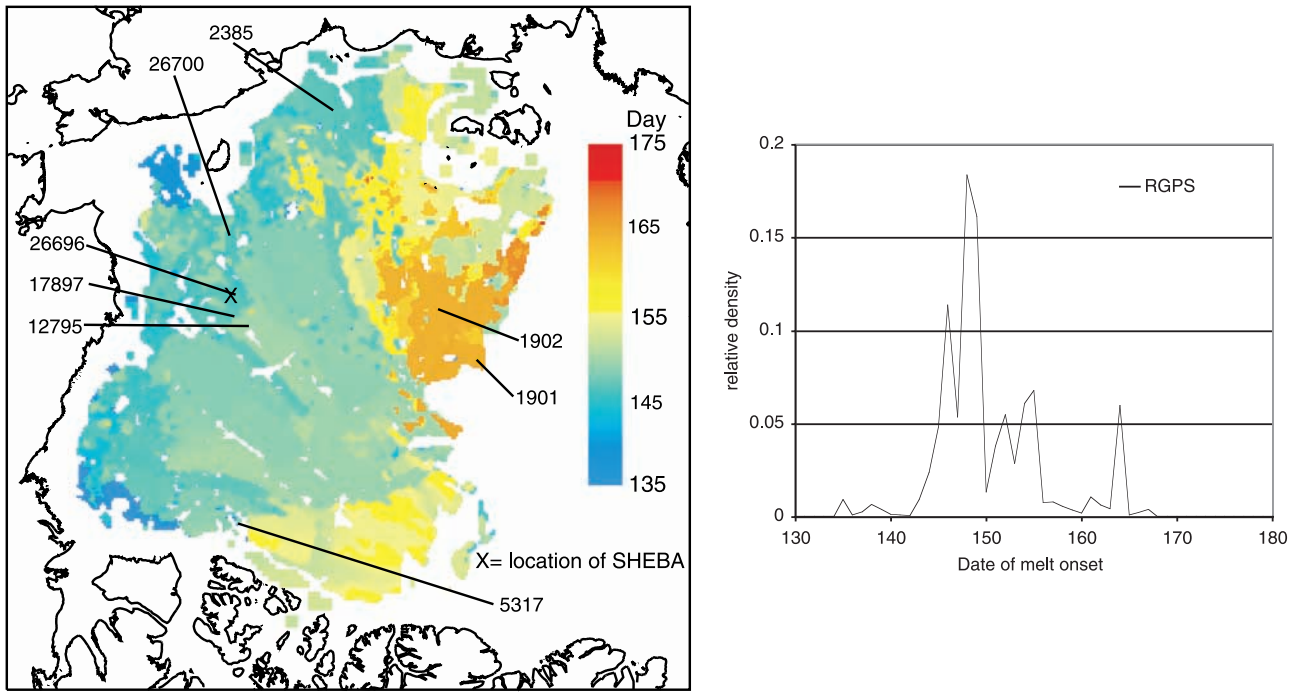

Figure 8. (a) Spatial pattern and (b) histogram of onset dates derived from the RGPS data set. Also shown are the locations of the eight IABP buoys within the RGPS area. Only buoys providing a complete temperature record throughout the melt onset period are used.

the Canadian Archipelago into the Canada Basin. Again, the passage of this system across the Arctic ice pack directly corresponds with the melt onset time detected in the portion of Figure 8 above Ellesmere Island. We also note the large low-pressure system that moved into the central Arctic during this latter time period. Apparently this large system was either too dry and/or too cold to begin melt onset in the remainder of the Arctic Basin covered by this study.

4.3. Comparison With Other Data Sets

[23] As a validation of the results, we compare the dates of melt onset derived here with zero-crossing dates of the air temperature measurements from individual buoy records. The locations of the eight buoys with a complete temporal record throughout the melt onset period and within the RGPS domain are shown in Figure 8. The comparisons are shown in Figure 11. In all cases, the results show that the onset dates are within 1–2 days of the initial zero-crossing dates from the buoy temperature records. We believe the primary source of uncertainty arises from the limited temporal resolution of the data–the nominal sampling period of the RGPS cells is 3 days. Thus the uncertainty in the melt onset dates would be ±1.5 days from the effects of temporal sampling. As pointed out by *Winerbrenner et al.* [1994], diurnal changes in backcatter are another possible source of uncertainty. As all our imagery is acquired during descending passes (~6:00 am local time), we do not think that diurnal effects are a problem in our analyses.

[24] We also compare our results with the melt onset dates derived from time series of SSM/I brightness temperature observations [*Drobot and Anderson*, 2001b]. The onset dates are derived using an algorithm detailed by *Drobot and Anderson* [2001a]. Figure 9 shows the SSM/I onset map, its histogram, and the map and histogram of the differences. There is a mean difference of ~7 days (later than the RGPS onset) with a standard deviation of ~2.5 days. The SSM/I derived onset map is generally noisier. Broadly speaking, there is general agreement in the pattern (yellow = zero difference) and the timing of melt between the RGPS and SSM/I analyses as indicated by the relatively large peak in the difference histogram. The difference seen in the comparison is due to regions with very late onset dates embedded in large regions that have already experienced onset in the SSM/I field. For example, in the Canada Basin where the RGPS results show a relatively uniform region with a narrow range of onset dates, the SSM/I algorithm detected onset dates that occur 15–20 days later than that estimated in the SAR data. The same is true for the northern central Eurasian Arctic (west of Wrangel) where the onset dates are later than that detected in the RGPS data. *Forster et al.* [2001] also noted this difference between the detected onset dates in active and passive microwave fields. This could be due to diurnal effects in the passive microwave data, and issues associated with coarse spatial resolution of the sensors. Specifically, the time series of brightness temperatures at fixed geographic locations in the gridded fields consist of contributions from varying areal fractions of different ice types and open water because of divergence and advection of sea ice. Possibly, the melt signal could be delayed because of different effect of snow wetness on surface emissivity at the passive microwave wavelengths. These factors could cause variability in signatures that could confound the detection procedures.

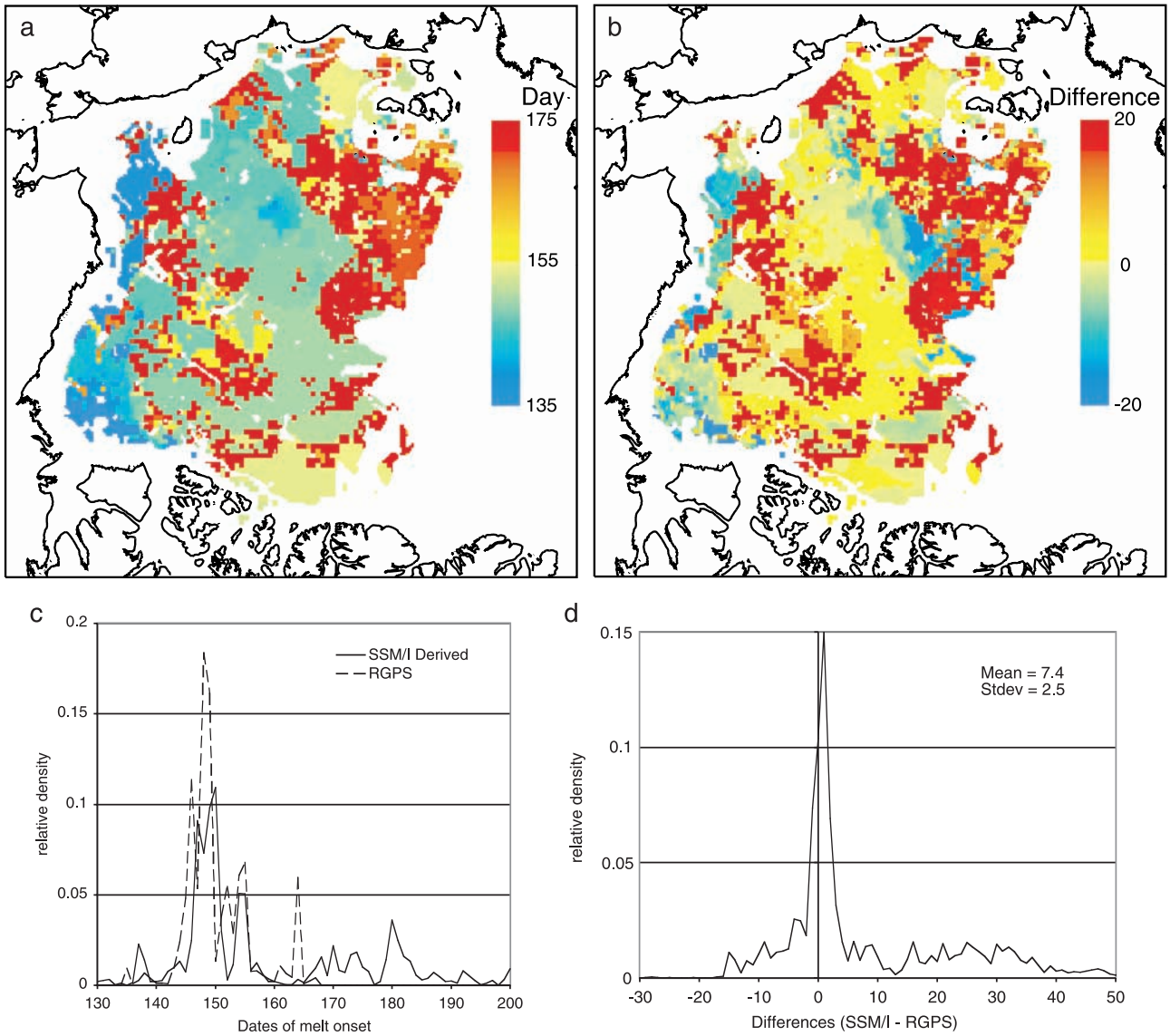

Figure 9. Comparison of RGPS and SSM/I onset dates. (a) Dates of melt onset derived from passive microwave observations [*Drobot and Anderson*, 2001b]. (b) Differences between SSM/I and RGPS onset dates. (c) Histogram of SSM/I (solid) and RGPS (dashed) onset dates. (d) Histogram of the differences between SSM/I and RGPS onset dates.

[25] Another hypothesis is that, at the wavelengths considered here, brightness temperature (T_B) measured by a radiometer is more dependent on the magnitude of the effective dielectric constant ($|\varepsilon_{eff}|$) of the surface snow layer while radar backscatter is more sensitive to the imaginary part ($Im\{\varepsilon_{eff}\}$) of the snow effective dielectric constant. A small amount of snow wetness occurring at or close to the zero crossing of the temperature record is sufficient to cause a significant change in $Im\{\varepsilon_{eff}\}$ resulting in a large change in backscatter [*Nghiem et al.*, 2001]. For the magnitude of $|\varepsilon_{eff}|$ to change significantly, a larger amount of wetness in the surface snow layer over an extensive area is necessary to cause significant changes in T_B and for the passive algorithm to detect effectively. Thus the melt detected by a radiometer may correspond to a later melt stage compared to an earlier stage of melt (near onset) detected by a radar. This is consistent with the delay in melt timing derived from passive SSM/I data compared to that obtained from active SAR data.

[26] Comparison of onset dates derived from SSM/I with zero crossing of the individual buoy temperature records (Figure 11) also corroborates the fact that the onset dates detected in SSM/I data all occur later than the initial zero crossings of the temperatures at the buoys and the RGPS estimates. Only four of the eight comparisons are within five days of the initial onset. Overall, this introduces a bias in the SSM/I results. The SSM/I detection algorithm seems to respond to the onset signal at a date sometime after the initial onset.

4.4. Comparison With Melt Onset in 1992: Beaufort Sea

[27] Here, we compare our onset dates with results from the spring of 1992 in the Beaufort Sea in Plate 1 of *Winebrenner et al.* [1994]. This is a comparison of results, derived from a C band radar (ERS-1 SAR) data set with similar characteristics, and with the same level of temporal sampling uncertainty.

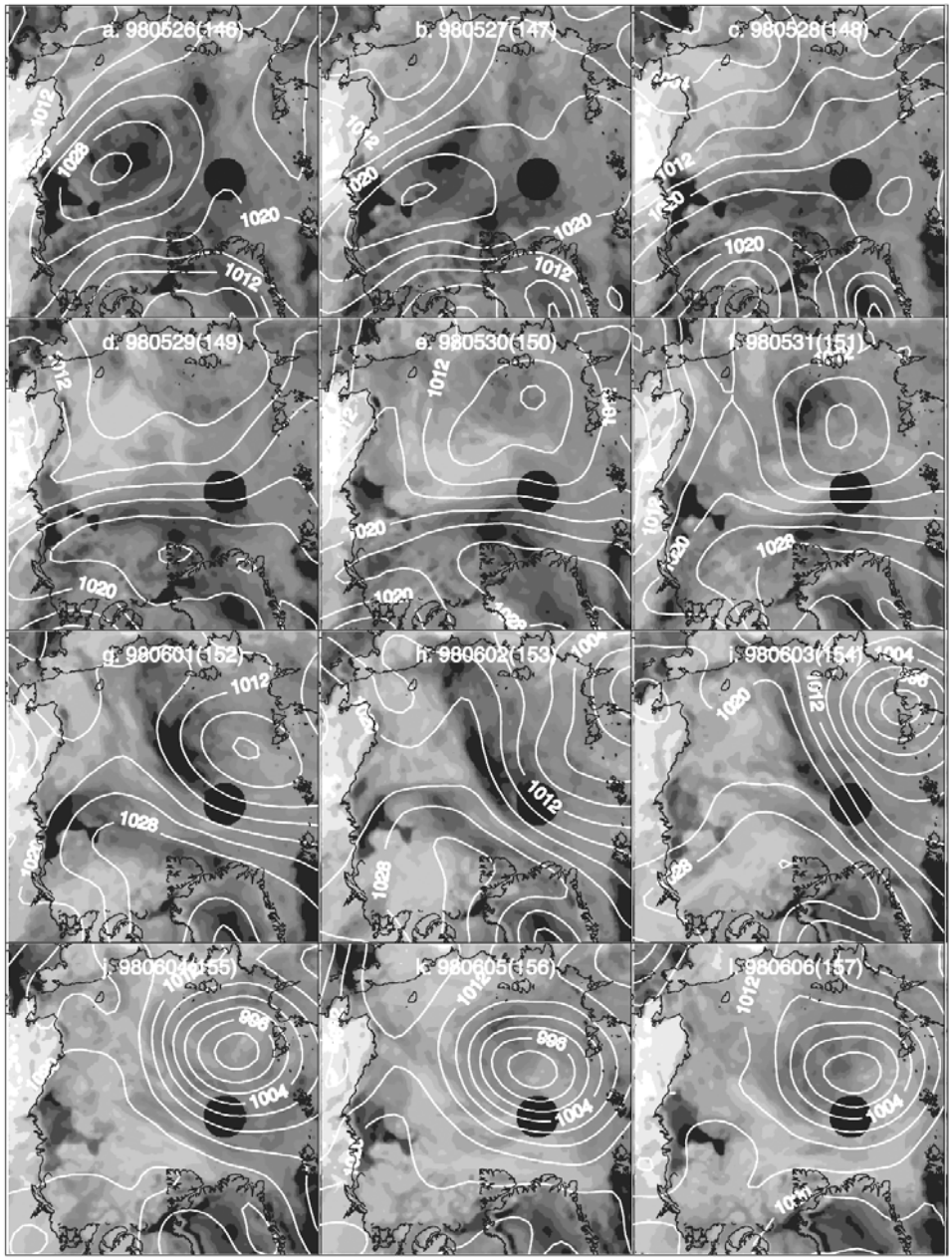

Figure 10. A 12-day sequence of 85 GHz (horizontal polarization) SSM/I maps with overlaid sea level pressure contours (contour interval 4 hPa) showing the development of the synoptic weather systems over the onset period (see discussion in text).

Over the same 21 sample regions (100 km by 100 km) in the Beaufort Sea as used by *Winebrenner et al.* [1994], the onset dates derived from the ERS data set ranges from 13 to 20 June in 1992 compared to that derived from the RGPS data set of 26–30 May in 1998. In 1998, the onset occurred two weeks earlier than that in 1992. This comparison is not intended to indicate a trend. However, over the two years it does highlight the range and variability in onset dates within a region as measured by high-resolution radar.

5. Conclusions

[28] The detection of melt onset in RGPS data over a large part of the Arctic during the spring of 1998 is studied. The sequence of Lagrangian observation of sea ice in RGPS data allows the systematic analysis of the changes in the area and backscatter of specific ice parcels over time. The time series of backscatter changes during melt onset is unique, as that ice area is not contaminated by variability due to ice characteristics and ice advection. This permits a better understanding of the consistency of the onset signatures. The onset signals of pure multiyear ice, as shown by *Winebrenner et al.* [1994], and first-year ice by *Barber et al.* [1995], are shown to be distinct in C band SAR data. Areas containing mixtures of MY and FY ice have onset signals that are dependent on the fractional coverage of these ice types. The behavior of the cell backscatter over the full range of ice mixtures can be observed in RGPS data.

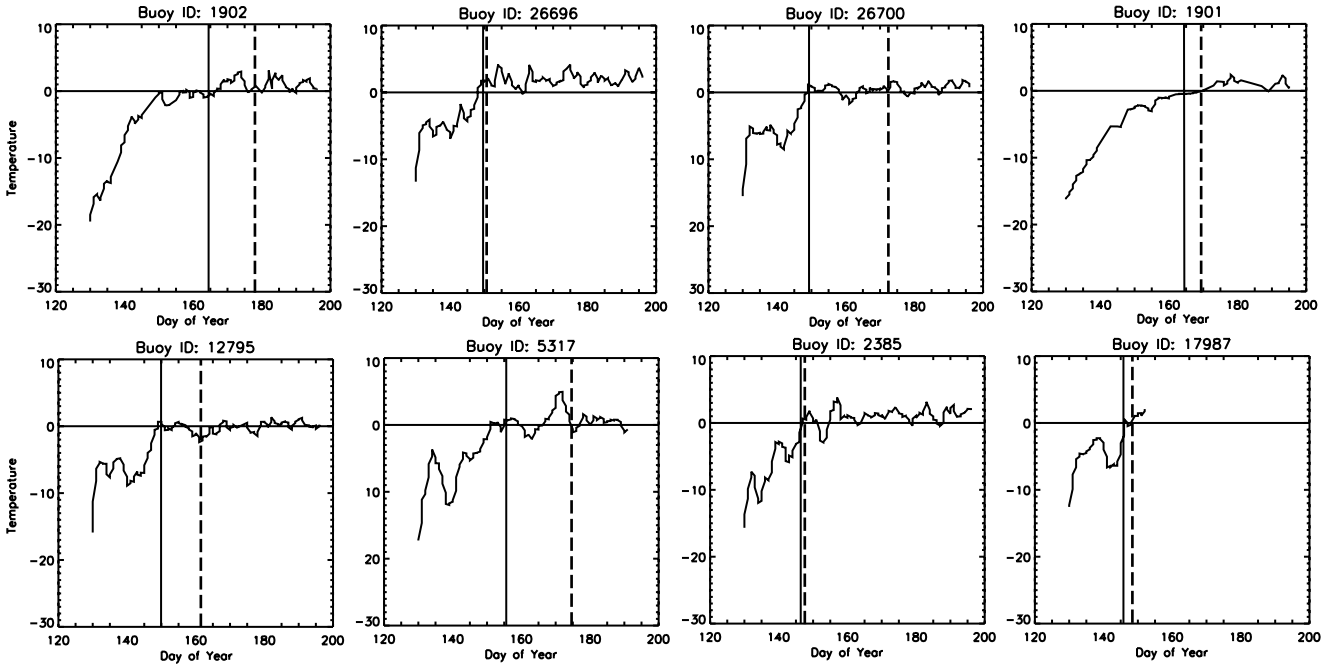

Figure 11. Comparison of RGPS and SSM/I-derived melt onset date with zero-crossing dates of individual buoy temperature records. The locations of the buoys are also shown in Figure 8. Solid and dashed vertical lines indicate the onset date derived from the RGPS and SSM/I data sets, respectively.

Indicators based on the characteristics of the backscatter distribution within an RGPS cell are devised to detect the melt onset signal. These indicators are robust: the map of the timing of melt onset is relatively uniform and there are no distinguishable boundaries between regions of predominantly FY and MY ice. During the spring of 1998, the spatial pattern of melt dates shows approximately three distinct regions with different onset dates (145–150, 150–155, and 162–166). The spatial patterns are highly coherent with fairly sharp boundary delineating the three regions. This distinctive pattern is correlated to warming due to an Arctic weather system seen at the end of May.

[29] The results are compared to the available in situ data of temperature, albedo and onset estimates derived from passive microwave data sets. Most importantly, there is close correspondence between the estimated timing of melt onset with the onset of albedo decrease measured at the SHEBA ice camp. Since our interest, in a radiative sense, is in using radar backscatter changes as a proxy indicator of the initial change in albedo associated with melt onset, this is an encouraging result. The estimated onset is within 1–2 days of the zero crossing of individual buoy temperature records. We attribute the larger difference between the RGPS estimates and that derived from passive microwave fields to be due to different sensitivity of the high-frequency radiometric measurements to the appearance of liquid water in the snow cover over sea ice, the variability of sea ice characteristics, and the coarser spatial resolution of the passive microwave sensors. Compared with the zero crossings of the temperature record of the drifting buoys, the uncertainties in the SAR derived onset are much lower than that of the passive microwave fields.

[30] This is the first of such fields derived from RADARSAT data. Of more geophysical interest is the accumulation of a long record of such fields to observe interannual variations and trends in times and locations of melt onset. At this writing, five years of RADARSAT data suitable for such analyses have been collected and such fields of onset dates will be produced as the RGPS data sets become available.

Appendix A: Onset Detection Algorithm

[31] On the basis of the behavior of the melt signal as depicted in Figures 6 and 7, we describe our detection algorithm using the sequences of σ, f, and P. The algorithm checks for significant changes in the three metrics derived from the record of backscatter histograms of each RGPS cell. Filters are first applied to each sequence to remove cells with large observational gaps (>7 days) and cells with large divergence/convergence (>25%). To reduce computation requirements, the procedure is applied only when the air temperature is $>-5^{\circ}$C.

[32] Figure 7 serves as a guide for derivation of the threshold values used in the detection process. Many image sequences, such as those in Figure 3, were examined to verify the effectiveness of these values presented below. The parameters are then adjusted to minimize the noise in the detection process. The detection of onset in the three metrics follows the four decision rules below:

A1. Detection of Onset in σ

[33] Within a sequence of backscatter observations, we examine consecutive runs of either all increasing or all decreasing mean backscatter. Onset is detected if the $\Delta\sigma$ of a run exceeds a prescribed C_{MY}-dependent threshold, $\Delta\sigma_{on}$. The two endpoints of the linear function are $\Delta\sigma_{on}(C_{\mathrm{MY}} = 0.0) = +2$dB and $\Delta\sigma_{on}(C_{\mathrm{MY}} = 1.0) = -3$ dB. The interpolated onset date is then set to be the point where the backscatter is $0.6\Delta\sigma_{on}$ above or below the first point of

that run. Further, this rule is applied only when ($\Delta\sigma > 0$ and $C_{MY} < 0.3$) or ($\Delta\sigma < 0$ and $C_{MY} > 0.4$). There are no restrictions on the sign of $\Delta\sigma$ when $0.3 < C_{MY} < 0.4$. These conditions require cells with low C_{MY} to exhibit an increase in σ while the opposite is expected for high C_{MY}. Otherwise, the behavior does not fit within our model of onset as summarized in Figure 7.

A2. Detection of Onset in f

[34] Here, changes in f between sequential observation pairs are examined. Onset is detected if a change in f exceeds a C_{MY}-dependent threshold, Δf_{on}, where endpoints of the linear function are $\Delta f_{on}(C_{MY} = 0.0) = 0.15$ and $\Delta f_{on}(C_{MY} = 1.0) = -0.5$. The interpolated onset date is then the point where f is $0.4\Delta f_{on}$ above or below the first point of that pair. Since large Δf over an observation pair may be obscured when the time separation (Δt) is small, we also examine the rates of change. If the daily change in f exceeds a linear threshold $0.25\Delta f_{on}$, onset is detected. The interpolated onset date is then set to be the point where f is $0.4\Delta f_{on}$ above or below the initial point. If both criteria are satisfied, the earlier of the two onset dates is kept. This rule is applied only when ($\Delta f > 0$ and $C_{MY} < 0.25$) or ($\Delta f < 0$ and $C_{MY} > 0.45$). This rule is not used when $0.25 < C_{MY} < 0.45$, as Δf is sensitive to small changes in σ when the cell backscatter is close to σ_{th} defined previously. Similarly, these conditions require cells with low C_{MY} to exhibit an increase in f while the opposite is expected for high C_{MY}.

A3. Detection of Onset in P

[35] This rule is effective in cases where the cells have a relatively even mixture of FY and MY ice. During onset, the mean backscatter within a cell does not change appreciably as the backscatter of MY and FY populations converge because of reversal and reduction in contrast. This results in an increase in the peak of the backscatter histogram of the cell. Here, the time sequence of P is examined over consecutive observations and onset is detected if a change exceeds a prescribed C_{MY}-dependent threshold, ΔP_{on}. The endpoints of the linear function are $\Delta P_{on}(C_{MY} = 0.0) = 0.09$ and $\Delta P_{on}(C_{MY} = 1.0) = 0.12$. The interpolated onset time is then set to where P is $0.4\Delta P_{on}$ above the initial point. As with f, the daily change P is also checked against $\Delta P_{on} = 0.25P_{on}$. If this ΔP_{on} is exceeded, the interpolated date is set to $0.4\Delta P_{on}$ above the initial point. If both criteria are satisfied, the earlier of the two dates is kept.

[36] If onset is detected in all three of the metrics and the dates are within six days of each other, the average of the two closest dates is deemed the date of melt onset. Otherwise, we select the earliest melt signal to avoid large fluctuations in backscatter signature that would trigger false alarms at dates after the initial onset when the ice cover melts and drains or pools.

[37] **Acknowledgments.** The RADARSAT imagery are processed and calibrated at the Alaska SAR Facility, Fairbanks, AK. The RGPS is a joint project of the Alaska SAR Facility and the Jet Propulsion Laboratory. These RGPS data sets are available on the Web (URL: http://www-radar.jpl.nasa.gov/rgps/radarsat.html). The SMMR and SSM/I brightness temperature and ice concentration fields are provided by World Data Center A for Glaciology/National Snow and Ice Data Center, University of Colorado, Boulder, CO. R. Kwok, G. F. Cunningham, and S. V. Nghiem performed this work at the Jet Propulsion Laboratory, California Institute of Technology under contract with the National Aeronautics and Space Administration.

References

Anderson, M. R., The onset of spring melt in first-year ice regions of the Arctic as determined from scanning multichannel microwave radiometer data for 1979 and 1980, *J. Geophys. Res.*, *92*, 13,153–13,163, 1987.

Anderson, M. R., Determination of melt onset date for Arctic sea ice regions using passive microwave data, *Ann. Glaciol.*, *25*, 382–387, 1997.

Anderson, M. R., and S. D. Drobot, Spatial and temporal variability in snowmelt onset over Arctic sea ice, *Ann. Glacio.*, *33*, 74–78, 2001.

Ball, G. H., and D. J. Hall, A clustering technique for summarizing multivariate data, *Behav. Sci.*, *12*, 143–155, 1967.

Barber, D. G., T. N. Papakyriakou, E. F. LeDrew, and M. E. Shokr, An examination of the relationship between spring period evolution of the scattering coefficient (σ°) and radiative fluxes over landfast sea-ice, *Int. J. Remote Sens.*, *16*, 3343–3363, 1995.

Drobot, S. D., and M. R. Anderson, An improved method for determining snowmelt onset dates over Arctic sea ice using scanning multichannel microwave radiometer and Special Sensor Microwave/Imager data, *J. Geophys. Res.*, *106*, 24,033–24,049, 2001a.

Drobot, S., and M. R. Anderson, Snow melt onset over arctic sea ice from SMMR and SSM/I brightness temperatures, Natl. Snow and Ice Data Cent., Boulder, Colo., 2001b. (Available as http://www.nsidc.org/data/nsidc-0105.html).

Forster, R. R., D. G. Long, K. C. Jezek, S. D. Drobot, and M. R. Anderson, The onset of Arctic sea-ice snowmelt as detected with passive- and active-microwave remote sensing, *Ann. Glaciol.*, *33*, 85–93, 2001.

Kwok, R., The RADARSAT Geophysical Processor System, in *Analysis of SAR Data of the Polar Oceans: Recent Advances*, edited by C. Tsatsoulis and R. Kwok, pp. 235–258, Springer-Verlag, New York, 1998.

Kwok, R., and G. F. Cunningham, Seasonal ice area and volume production of the Arctic Ocean: November 1996 through April 1997, *J. Geophys. Res.*, *107*(C10), 8038, doi:10.1039/2000JC000469, 2002.

Kwok, R., D. A. Rothrock, H. L. Stern, and G. F. Cunningham, Determination of ice age using Lagrangian observations of ice motion, *IEEE Trans. Geosci. Remote Sens.*, *33*, 392–400, 1995.

Nghiem, S. V., and C. Bertoia, Study of multi-polarization C-band backscatter signatures for Arctic sea ice mapping with future satellite SAR, *Can. J. of Remote Sens.*, *27*, 387–402, 2001.

Nghiem, S. V., K. Steffen, R. Kwok, and W.-Y. Tsai, Detection of snowmelt regions on the Greenland ice sheet using diurnal backscatter change, *J. Glaciol.*, *47*, 539–547, 2001.

Perovich, D. K., T. C. Grenfell, B. Light, J. A. Richter-Menge, M. Sturm, W. B. Tucker III, H. Eicken, and G. A. Maykut, *SHEBA: Snow and Ice Studies* [CD-ROM], Cold Reg. Res. Lab., U. S. Army Corp of Eng., Hanover, N. H., 1999.

Rigor, I., R. Colony, and S. Martin, Variations in surface air temperature observations in the Arctic, 1979–1997, *J. Clim*, *13*, 896–914, 2000.

Smith, D. M., Observations of perennial Arctic sea ice melt and freeze-up using passive microwave data, *J. Geophys. Res.*, *103*, 27,753–27,769, 1998.

Thomas, A., and D. G. Barber, On the use of multi-yea ice ERS-1 σ_o as a proxy indicator of melt period sea ice albedo, *Int. J. Remote Sens.*, *19*, 2807–2821, 1998.

Winebrenner, D. P., E. Nelson, R. Colony, and R. West, Observation of melt onset on multiyear Arctic sea ice using ERS-1 synthetic aperture radar, *J. Geophys. Res.*, *22*(99), 22,425–22,441, 1994.

Winebrenner, D. P., D. G. Long, and B. Holt, Mapping the progression of melt onset and freeze-up on Arctic sea ice using SAR and scatterometry, in *Analysis of SAR Data of the Polar Oceans: Recent Advances*, edited by C. Tsatsoulis and R. Kwok, pp. 129–144, Springer-Verlag, New York, 1998.

G. F. Cunningham, R. Kwok, and S. V. Nghiem, Jet Propulsion Laboratory, California Institute of Technology, 4800 Oak Grove Drive, Pasadena, CA 91109, USA. (ron.kwok@jpl.nasa.gov)